




Article

Synchronised TeraHertz Radiation and Soft X-rays Produced in a FEL Oscillator

Vittoria Petrillo ^{1,2,*}, Alberto Bacci ², Illya Drebot ², Michele Opromolla ^{1,2}, Andrea Renato Rossi ² ,
Marcello Rossetti Conti ² , Marcel Ruijter ², Sanae Samsam ^{2,3} and Luca Serafini ² 

¹ Department of Physics, Università degli Studi di Milano, Via Celoria 16, 20133 Milan, Italy

² Istituto Nazionale di Fisica Nucleare-Sezione di Milano, Via Celoria 16, 20133 Milan and LASA, Via F. Cervi 201, 20090 Segrate (MI), Italy

³ Università di Roma "La Sapienza", Piazzale Aldo Moro 5, 00185 Rome, Italy

* Correspondence: vittoria.petrillo@mi.infn.it

Abstract: We present a scheme to generate synchronised THz and soft X-ray radiation pulses by using a free-electron laser oscillator driven by a high repetition rate (of order 10–100 MHz) energy recovery linac. The backward THz radiation in the oscillator cavity interacts with a successive electron bunch, thus producing few 10^5 soft/hard X-ray photons per shot (namely 10^{12} – 10^{13} photons/s) via Thomson/Compton back-scattering, synchronised with the mJ-class THz pulse within the temporal jitter of electron beams accelerated in the superconducting cavities of the linac (less than 100 fs). Detailed simulations have been performed in order to assess the capability of the scheme for typical wavelengths of interest, between 10 and 50 μm for the TeraHertz radiation and 0.5–3 nm for the X-rays.

Keywords: FEL oscillator; Compton source; dual source



Citation: Petrillo, V.; Bacci, A.; Drebot, I.; Opromolla, M.; Rossi, A.R.; Rossetti Conti, M.; Ruijter, M.; Samsam, S.; Serafini, L. Synchronised TeraHertz Radiation and Soft X-rays Produced in a FEL Oscillator. *Appl. Sci.* **2022**, *12*, 8341. <https://doi.org/10.3390/app12168341>

Academic Editor: Edik U. Rafailov

Received: 21 June 2022

Accepted: 17 August 2022

Published: 20 August 2022

Publisher's Note: MDPI stays neutral with regard to jurisdictional claims in published maps and institutional affiliations.



Copyright: © 2022 by the authors. Licensee MDPI, Basel, Switzerland. This article is an open access article distributed under the terms and conditions of the Creative Commons Attribution (CC BY) license (<https://creativecommons.org/licenses/by/4.0/>).

1. Introduction

Fundamental and applied studies at the science frontiers need tuneable, brilliant and coherent radiation pulses. The synchronised radiation of two different wavelengths is required for testing phenomena developing on different time-scales or for pump and probe experiments, where one of the two pulses excites microscopic processes and the other one detects them. The combination of strong THz excitation sources with the most advanced X-ray light sources enables the study of long-range order at atomic length scales and ultra-fast time-scales [1,2]. The expectation of experiments of this kind is so promising that almost all the laboratories allocating the most brilliant X-ray sources, namely synchrotrons and free-electron lasers (FELs), are also endowed with THz sources to be coupled with the X-rays [3,4]. However, when these experiments involve Synchrotrons and FELs as sources of X-rays, they can be exclusively carried out in a poorly sustainable way in few huge laboratories, limiting the widespread diffusion of this research technique. Regarding the generation of THz radiation, considerable efforts are currently being made to develop novel high-power radiation sources able to compensate for the scarce availability in this frequency range. Much interest has been focused on FELs, because they are widely tuneable in the THz range and deliver high-quality pulses that satisfy the requirements of energy stability, polarisation, spectral and spatial distribution posed by the most advanced applications. Far-infrared and THz FELs mainly operate as oscillators, i.e., they are equipped with resonators confined by mirrors. The main advantages of this operational mode, with respect to other FEL configurations, are compactness, relaxed requirements of the electron bunch quality and the fact that oscillators are suitable for superconducting (SC) linacs, allowing the generation of powerful quasi-cw light. Such a class of FELs includes UCSB-FEL [5], CLIO [6], FELIX [7], FELBE [8], NovoFEL [9], KAERI-FEL [10] and ISIR FEL [11]. Among them, FELBE, which relies on a superconducting RF linac operated in the cw mode,

and UCSB-FEL, based on an electrostatic Van de Graaff accelerator with energy recovery operated in a long pulse mode, are characterised by the highest power yield. CLIO, FELIX, and ISIR FEL generate maximum micropulse energies between 100 and 40 μJ in the mid-infrared region, while their energies in the THz region decrease to values between 20 and 5 μJ . NovoFEL consists of a series of 180 MHz normal conducting RF cavities and an energy recovery system operating in the cw mode that can generate an average power of 400 W and a micropulse energy of 50 μJ . Various new projects [12–14] or studies involving THz FELs have been proposed [15,16].

The dual source (THz plus X-rays) that we expose in this paper exploits the fact that the THz radiation generated by the passage of successive electron bunches in an FEL undulator, driven by a super-conducting ERL, propagates at each round trip inside the cavity, first forward towards the front mirror and then backward to the rear mirror. After being reflected by a tilted front mirror, the radiation is sent obliquely off-axis with respect to the electron beam train and hits a successive electron bunch in a condition suitable for Thomson/Compton back-scattering. THz FEL intracavity pulses with mJ-class energy at 15–50 microns of wavelength, driven by 20–100 MeV energy electron bunches, can deliver up to few 10^5 soft X-ray photons per shot by Compton back-scattering at a rate of 10–100 MHz and synchronised with the THz radiation. The total of 10^{12} – 10^{13} X photons generated per second can be useful in many imaging fields (see Ref. [17]). Even taking into account size and cost of the cryogenic plant, this source is more compact (hundreds instead of tens of thousands square meters) and less expensive (less than one hundredth of the costs) than synchrotrons and soft X-ray FELs. It can therefore be developed in medium size laboratories, big hospitals or university campuses and represents an elementary upgrade of a basic THz FEL oscillator. Section 2 describes the generalities of the double source constituted by a THz free-electron laser oscillator and by a X-ray Thomson/Compton source driven by the same electron beam. Section 3 presents the THz free-electron laser oscillator, focusing the attention on geometry and working points suitable for this particular operation. Section 4 gives the details of the THz optical cavity. Section 5 provides an overview of the X-ray production by means of Thomson/Compton scattering. Finally, we conclude presenting considerations about the optimal layout, characterisation and performances of the dual source providing simultaneous THz and Soft X-ray radiation and discussing the possibility of developing such a device.

2. Double Source Constituted by a THz FEL Oscillator and a Thomson/Compton Source Driven by the Same Electron Beam: Generalities

In this section, we will determine the parameters of a THz FEL oscillator alimented by an electron beam accelerated by a Super Conducting (SC) Energy Recovery Linac (ERL) [18,19]. An SC accelerator is required because the FEL oscillator is based on the passage of successive electron beams at a large repetition rate inside the undulator. Moreover, the energy recovery option allows for a sustainable approach to the radiation generation. We based our study on an ERL similar to those described in [13,14,20]. A DC gun, JLab-like, equipped with solenoid and bunchers, guarantees low-emittance and a large repetition rate. The average current was maintained below 7–8 mA. The instabilities connected to the high-order modes are taken under control by a suitable design of the cavities [21,22], together with the insertion of dumpers. Table 1 presents values of the electron beam parameters given by start-to-end simulations, generated by Superconducting Linacs operating at the aforementioned energies (see also [5,8,14,21]). The table reports the slice emittance and energy spread values, since, in the FEL process, only the characteristics of the core of the electron beam are significant. The electron beam provides THz radiation with interesting properties and, at the same time, suitable for driving Thomson back-scattering. Even if the interaction is in the classical range (Thomson regime), following the usual lexicon in the field, we will also refer to the process as inverse Compton (or simply Compton) scattering.

Table 1. Electron beam characteristics at the undulator entrance.

Quantity	Before the Undulator
Energy	20–100 MeV
Charge	100–200 pC
Energy spread	0.1–1%
Slice emittance	0.6–2 mm mrad
Transverse size σ_x	0.1–0.25 mm
Length σ_z	0.5–5 mm
Average current	<7–8 mA

The accelerated electron bunches, travelling through the undulator, produce THz FEL radiation that is then reflected backward by the front mirror.

The total distance travelled by the radiation L_{rt} back and forth in the cavity and the repetition rate of the electron bunch train f must be connected in such a way that the radiation arrives exactly synchronised to a successive electron beam at the entrance of the undulator after a round trip: L_{rt} should therefore be a multiple of the distance between two successive bunches $L_{rt} = v_e/f$, v_e being the electron bunch velocity. Figure 1 shows an option based on a four-mirror cavity of the radiation source layout. The THz radiation produced by the FEL undulator propagates freely up to the tilted front mirror. Here, it is reflected off-axis and then obliquely sent to the Compton interaction point (IP) by a second mirror. The interaction therefore takes place at a small angle. The THz radiation is then shifted laterally by a few centimetres, thus circumventing the undulator. The focusing needed for increasing the luminosity of the process is provided by the mirrors surrounding the IP. This configuration is quite usual in Thomson/Compton sources based on lasers in Fabry–Perot cavities [20,23,24]. In addition, $L_{rt} = n\Delta l$ (n integer), Δl being the electron bunch-to-bunch inter-distance. If $n > 1$, more than one electron beam is simultaneously present inside the cavity. The Compton IP is set in a position where the length L_c of the path the radiation covers for coming back to this same point after the reflection equals a multiple of the distance between two electron bunches, i.e., $L_c = n'\Delta l$ (n' integer). The THz radiation, propagating backward, crosses a successive electron bunch and scatters X-ray radiation in the direction of the electrons at the same repetition rate. The X-ray and THz radiation that flow through the front mirror are generated in sequence by two successive bunches of the electron beam train and are therefore naturally synchronised within the characteristic temporal jitters of the SC accelerator.

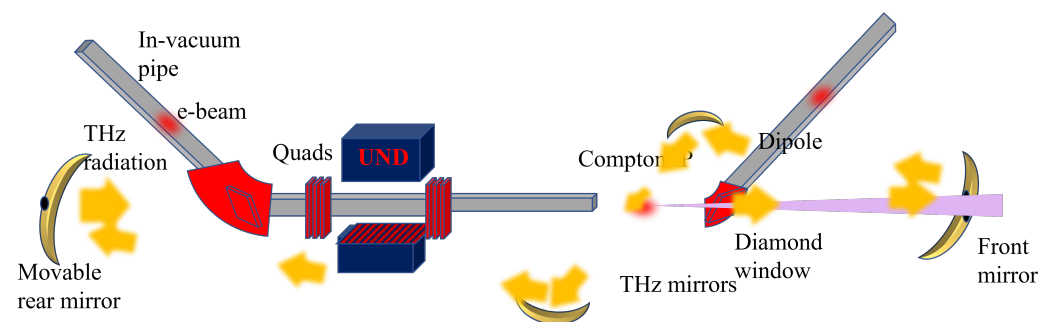


Figure 1. Dual source of THz and X-ray radiation. The cavity is constituted by four mirrors, one of them holed or translucent. The Compton interaction point is on the right, and the focusing is realised by the mirrors themselves. Electron beam and THz radiation interact at angle.

The possible combinations of THz and X-ray wavelengths produced by the device are analysed in Figure 2. The resonance condition of the FEL oscillator is $\lambda_{THz} = \lambda_w(1 + a_w^2)/(2\gamma^2)$, where $\gamma = E/mc^2$ is the Lorentz factor of the electron beam, λ_w and $a_w = eB\lambda_w/(\sqrt{22}\pi mc)$ the period and the undulator parameter (B is the undulator peak on-axis magnetic field), being m , e and c the electron rest mass, charge and the speed of light, respectively.

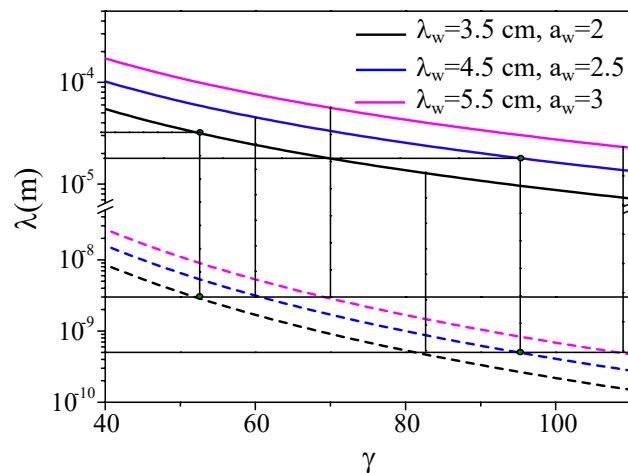


Figure 2. Wavelength of the THz and X-ray radiation vs. electron Lorentz factor γ . Solid lines: THz radiation produced with the FEL oscillator. Dashed lines: X-ray radiation generated by means of Thomson back-scattering. In black: $\lambda_w = 3.5$ cm, $a_w = 2$; similar values can also be obtained with $\lambda_w = 4.5$ cm, $a_w = 1.7$. In blue: $\lambda_w = 4.5$ cm, $a_w = 2.5$. In magenta: $\lambda_w = 5.5$ cm, $a_w = 3$.

Figure 2 shows the resonant values λ_{THz} as a function of the electron beam Lorentz factor γ ranging from 40 (20 MeV) to 110 (55 MeV), for various values of the undulator period λ_w between 3.5 cm and 5.5 cm at values of a_w between 2 and 3, respectively. As shown herein, the undulator can be tuned to cover a wide THz wavelength range with relatively low electron energy values. The intermediate value $\lambda_w = 4.5$ cm, for instance, allows to span the THz wavelengths from 100 to 35 μm , only varying the electron energy from approximately 20 to 50 MeV. By changing a_w , a wider range of wavelengths can be produced.

In the same graph, the Compton radiation wavelength $\lambda_X \simeq \lambda_{THz}/(4\gamma^2)$ generated by the scattering between the electron beam and the THz pulses is also presented (dotted lines), thus showing the couples of THz/X-ray wavelengths simultaneously generated. Interesting wavelengths in the soft-tender X-ray regime are, for instance, the water window at $\lambda = 3$ nm [25] or the spectroscopy range around 0.5 nm [26]. THz radiation at 30–55 μm can be paired with X-rays in the water window at 3 nm. With the same undulator, THz radiation in the range 13–25 μm generates X rays at $\lambda = 0.5$ nm. Long wavelength FEL radiation pulses present strong diffraction, which limits the minimum value that undulator periods and gaps can assume. The slippage along the propagation direction is moreover large and causes the possible transition to the superradiant regime [27,28], where the emitted energy is proportional to the square of the charge. In order to avoid the strong spectrum deterioration by deep radiation saturation, an electron beam rms length σ_e of the order of two times the slippage length $L_s = N_w \lambda_{THz}$ (N_w being the number of periods of the undulator module) could individuate a suitable working point satisfying the condition: $\sigma_e \geq 2L_s$. We can then determine the necessary undulator length. Following the road map proposed in [29] and references therein, another condition of operation threshold can be determined, i.e., $0.27(4\pi\rho)^3 N_w^3 > Loss$ where ρ is the Pierce parameter of the FEL [30,31] and loss is the percentage of energy lost by the light during the round trip from the end to the entrance of the undulator. This condition holds when the electron beam is much longer than the cooperation length $L_c = \lambda/(4\pi\rho)$, i.e., when $\sigma_e \gg L_c$ (long-bunch limit). The opposite limit features a different scaling law, leading to a slightly different threshold. If σ_e is about 5–10 times the cooperation length, the effective operative condition lays in an intermediate region between the two limiting cases ruled by the short and the long-bunch models. The radiation Rayleigh length Z_R should be of the order of half the undulator length and the dimension of the radiation beam turns out to be of the order of $\sigma_r \simeq \sqrt{\frac{Z_R \lambda}{2\pi}} \gg \sigma_e$. For this reason, since the radiation transverse size is much larger than the electron beam's size, even if the radiation losses due to the interaction with the mirrors

and to the pulse extraction along the trajectory outside the undulator are relatively small, and the electron beam-radiation coupling at the undulator entrance can be scarce. For instance, typical values of the radiation size are approximately 3 mm, while the electron radius is 100–200 μm , leading to an estimate of loss as large as approximately 99%. The number of undulator periods N_w satisfying the aforementioned constraint is $N_w > \frac{1.54}{4\pi\rho}$ in the case of a long bunch, or $N_w > \frac{1.18}{4\pi\rho}$ with a short electron beam.

The graph in Figure 3 presents the required undulator length $L_{und} = \lambda_w N_w$ as a function of the beam peak current $I(\text{A})$ for five cases based on two different undulator periods, where three-dimensional and inhomogeneous effects were taken into account in the calculation of the Pierce parameter as in Ref. [32]. Both long (solid lines) and short (dotted lines) electron beam cases are reported in the graph. Sustainable undulator lengths and reasonable peak currents ($7 \text{ A} < I < 25 \text{ A}$) in the range attainable by a SC high repetition rate accelerator are needed. Electron beams with 150 pC of charge, 15–20 A of peak current, reasonable values of emittance ($< 2 \text{ mm mrad}$) and energy spread ($< 5 \times 10^{-3}$) could produce more than 1 mJ of intra-cavity (IC) radiation energy at 10–50 μm of wavelength in less than 2 m of undulator, generating extra-cavity (EC) pulses of tens of μJ . The intra-cavity THz pulse constitutes the scattering radiation in the inverse Compton process, generating N_X photons at λ_X . The number of X-ray photons per shot N_X can be indeed roughly estimated as [33,34]:

$$N_X = \sigma_{Th} \frac{N_e N_{THz}}{2\pi(\sigma_e^2 + \sigma_{THz}^2)}. \quad (1)$$

where $\sigma_{Th} = 6.65 \times 10^{-29} \text{ m}^2$ is the Thomson cross-section, $N_e = Q/e = 1.25 \times 10^9$, $\sigma_e = 100 \mu\text{m}$, $N_{THz} = E_{IC}/(h\nu_{THz}) = E_{IC}\lambda_{THz}/(hc) \simeq 2\text{--}5 \times 10^{17}$, an amount of approximately 10^5 X-ray photons per shot is delivered by the system on the whole spectrum, provided that $\sigma_{THz} \leq 0.3 \text{ mm}$. At a repetition rate of approximately 50 MHz, the source could deliver to the users 5×10^{12} X-ray photons/s together with $2\text{--}5 \times 10^{23}$ THz photons/s. As can be seen by Equation (1), the reflected radiation must hit the electrons in the condition of maximum focusing to optimise the Compton scattering luminosity. For controlling the transverse size of the radiation, a telescopic system of lenses or mirrors should be put around the Compton IP. In the case of lenses, at least one of them should be holed for the passage of the X-rays, and the electron beam should circumvent the lenses. The loss of THz radiation transmission, which adds to the other cavity losses, can be estimated by the ratio between the hole surface (approximately given by the electron beam transverse dimension) and the lens illuminated area: in optimal conditions, it can be maintained under few percent due to the low X-ray diffraction. A deformation of the THz fields around the holes could also occur.

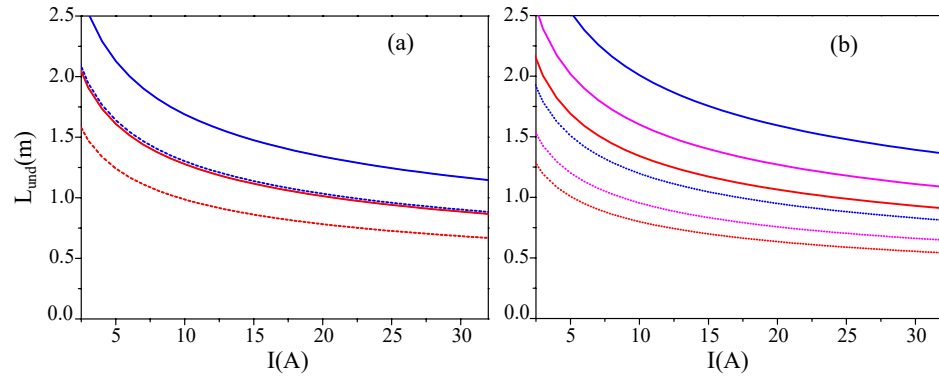


Figure 3. Undulator length L_{und} versus electron beam peak current $I(A)$. Solid curves represent the long bunch cases, dotted curves represent the short bunch cases. Window (a): $\lambda = 36 \mu\text{m}$, $\lambda_w = 3.5 \text{ cm}$, $\gamma = 55.5$ (red curves); $\lambda = 13.2 \mu\text{m}$, $\lambda_w = 3.5 \text{ cm}$, $\gamma = 81.5$ (blue curves). Window (b): $\lambda = 51.6 \mu\text{m}$, $\lambda_w = 4.5 \text{ cm}$, $\gamma = 65$ (red curve); $\lambda = 36 \mu\text{m}$, $\lambda_w = 4.5 \text{ cm}$, $\gamma = 55.5$ (magenta curves); $\lambda = 15 \mu\text{m}$, $\lambda_w = 4.5 \text{ cm}$, $\gamma = 86$ (blue curves). Three-dimensional and inhomogeneous effects are taken into account.

3. The THz FEL Oscillator: Numerical Results

In this section, we describe and discuss the simulation results of the THz FEL oscillator. The procedure follows the evolution of the radiation within the system composed by the cavity and the undulator. As a first step, the FEL emission is computed starting from noise in the undulator. The radiation electric field is extracted over a three-dimensional grid at the end of the undulator and transported through the cavity. After reflection by the rear mirror, the radiation pulse encounters a successive electron bunch and seeds it in the subsequent passage inside the undulator. The process is then reiterated up to saturation. The FEL simulation has been carried out by using the three-dimensional, time-dependent FEL code Genesis 1.3 [35]. The cycling of the radiation through the cavity has been evaluated by means of the Huygens integral [36–38], taking into account the losses on the optical elements and the geometry of the whole optical line. Besides the absorption of the optics and the effect of the holes, other losses come from the imperfect matching between radiation and electrons at the undulator entrance due to the natural difference in their transverse sizes. The THz radiation, in fact, arrives at the entrance of the undulator with a dimension much larger than the electron beam size, and only a fraction of its energy is coupled to and contributes to seed the particles. The profiles of the electron beam size matched to the undulator and of the radiation at a different round trip are presented along the undulator coordinate z , respectively, in Figures 4 and 5. The radiation starts at the beginning of the electron beam and diverges due to diffraction, but then achieves stationary behaviour on values determined by the cavity properties.

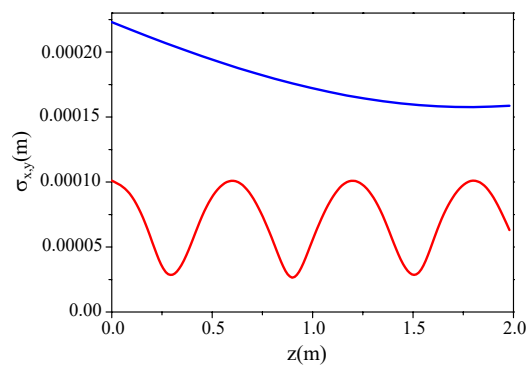


Figure 4. Electron sizes σ_x , (blue curve) and σ_y (red curve) (m) along the undulator coordinate $z(m)$ for $\lambda = 15.2 \mu\text{m}$, emittance $\epsilon = 1 \text{ mm mrad}$, loss = 6%.

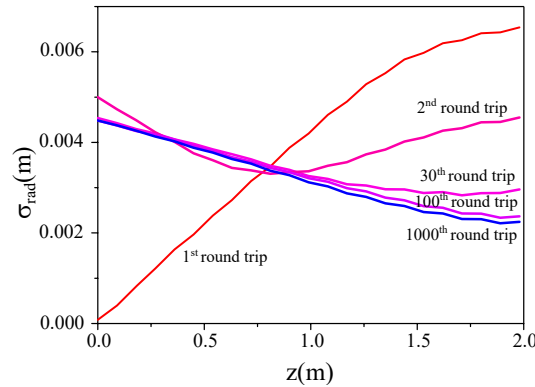


Figure 5. Radiation size σ_{rad} (m) along the undulator coordinate z (m) for $\lambda = 15.2 \mu\text{m}$, emittance $\epsilon = 1 \text{ mm mrad}$, loss = 6% for different round trip numbers.

The total losses $Loss$ are given by the sum of several terms, namely the fraction of energy extracted from the system $L_{ext} = E_{EC}/E_{IC}$, E_{IC} and E_{EC} being the intra-cavity and extra-cavity energies, the absorption of the mirrors L_{mirr} , the losses on the lenses and the effect of the holes L_{lens} , and the mismatch term L_{mm} estimated by $L_{mm} = 1 - A_e/A_{rad}$, where A_{rad} and A_e are the radiation and electron area at the beginning of the undulator, respectively. The last term, connected to the filling factor, is widely dominating. In order to take into account the jitters in energy of the linac, a sequence of electron bunches different ones from others both microscopically (by randomly changing the seed of the Hammersley sequences of the electron phase space distributions) and macroscopically, by preparing and injecting them into the undulator, thus simulating the shot-to-shot fluctuations of the bunch train. The macroscopic shot-to-shot variations of the average characteristics within the jitter intervals include the random change of the electron energy by 1 per mill, the tuning between electron beam and radiation within 100 fs of time delay, and the transverse overlapping with 50 μm of pointing jitter. Due to their different velocities, the radiation field travelling inside the cavity overtakes the electron beam. The pulse therefore needs to be delayed by the total slippage length at the successive round trip. Implementing a slight shortening of the cavity length, the radiation turns out to be synchronised with the next bunch at the undulator entrance and within the temporal jitter [39]. The value of the energy achieved at saturation as a function of the time delay between electrons and radiation is shown in Figure 6. The wide width of the curve is much larger than the time fluctuation of an electron beam train in an SC linac, less or at a maximum of the order of 100 fs.

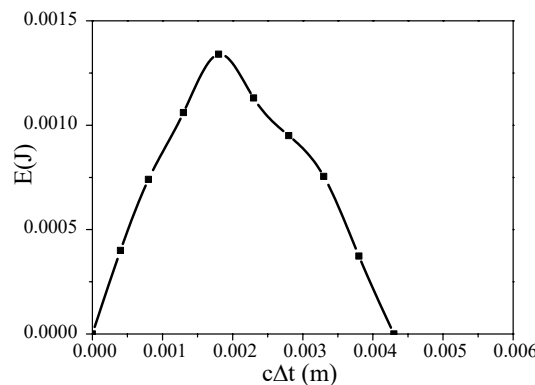


Figure 6. Intra-cavity radiation energy E (J) vs. time delay $c\Delta t$ (m) between electrons and radiation for radiation wavelength $\lambda = 15.2 \mu\text{m}$, emittance $\epsilon = 1 \text{ mm mrad}$, loss = 6%.

With the electron beam parameters in the range shown in Table 1, assuming the values of $Q = 250 \text{ pC}$, $I_{peak} = 20 \text{ A}$, $\epsilon_n = 1.4 \text{ mm mrad}$, energy spread $\Delta E = 100 \text{ keV}$ and varying energies with a jitter of 2×10^{-4} , five reference cases have been studied: two based on an undulator with a period $\lambda_w = 3.5 \text{ cm}$ and three with $\lambda_w = 4.5 \text{ cm}$. The data and the results

are summarised in Table 2. THz radiation energies larger than 1 mJ are always obtained for wavelengths between 13 and 50 μm , with undulator lengths larger than 1.5 m. Figure 7 shows the energy growth as a function of the round trip number inside the cavity for the five analysed cases, in the case of cavity losses at 2%. The radiation power profiles at saturation are instead shown in Figure 8. In some cases, the power shape is multi-spiky, resulting in a broad and polychromatic spectrum. In these cases, the long wavelength and the relatively longer undulator lead to a high total slippage, with the involvement of more supermodes [39–41]. Regarding the efficiency of the Compton scattering, these cases are characterised by larger energy levels and present advantages in terms of output flux, but their wider bandwidths limit the spectral density of the X-ray yield. We also varied the reflection coefficient of the mirrors in order to study different cavity options. Table 3 summarises the intra-cavity energy obtained with different values of cavity losses and electron emittances in the case of a wavelength at 15 μm . Figure 9 is relevant to the less advantageous case of Table 3, with total losses at 6% (2% of outcoupling and 4% of cavity dissipation) and an emittance of 1.4 mmrad and reports the gain $G = (E(L_{und}) - E(0))/E(L_{und})$ as function of the round trip number. At saturation, gain and losses are exactly balanced, while before saturation, the gain reaches 30%.

Table 2. THz radiation: undulator specifics, electron energy, and results (repetition rate at 5×10^7 Hz). E_{IC} and E_{EC} indicate the intra-cavity and extra-cavity radiation energy, respectively; size, div and P_{EC} are the output radiation size, divergence and the extra-cavity radiation power level, respectively. Mirror losses at 2%.

λ_w (cm)	3.5	3.5	4.5	4.5	4.5
a_w	2.33	2	2.95	2	2
L_{und} (m)	2	2	1.71	1.71	1.71
γ	55.5	81.5	65	55.5	86
λ_{THz} (μm)	36	13.2	51.6	36	15
E_{IC} (mJ)	3	3.38	1	2.1	2.8
E_{EC} (μJ)	60	67	20	42	56
bw (%)	4	2.6	1	2.5	2.15
size (mm)	2.7	1.6	3	3	2.2
div (mrad)	3.5	1.8	6	4	3.7
P_{EC} (kW)	3	3.4	1	2.1	2.8
λ_X (nm)	3	0.5	3	3	0.5

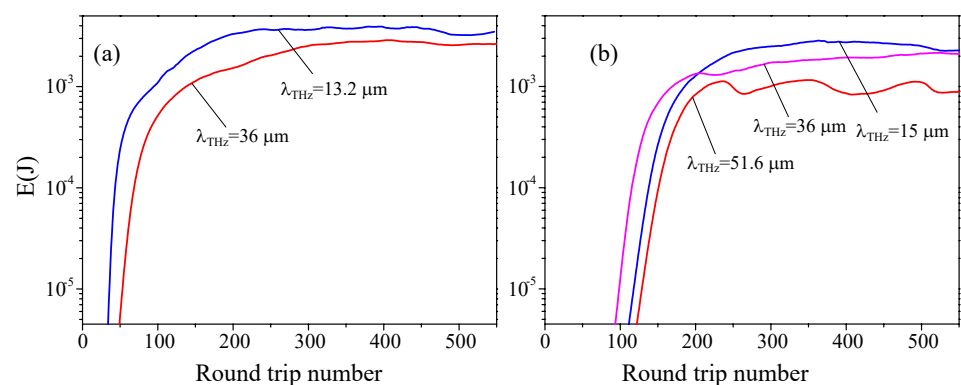


Figure 7. Intra-cavity radiation energy growth $E(J)$ vs. a number of shots N . Window (a): undulator period $\lambda_w = 3.5$ cm; red curve: $\gamma = 55.5$, $\lambda = 36$ μm ; blue curve: $\gamma = 81.5$, $\lambda = 13.2$ μm . Window (b): undulator period $\lambda_w = 4.5$ cm; red curve: $\gamma = 65$, $\lambda = 51.6$ μm ; magenta curve: $\gamma = 55.5$, $\lambda = 36$ μm ; blue curve: $\gamma = 86$, $\lambda = 15$ μm .

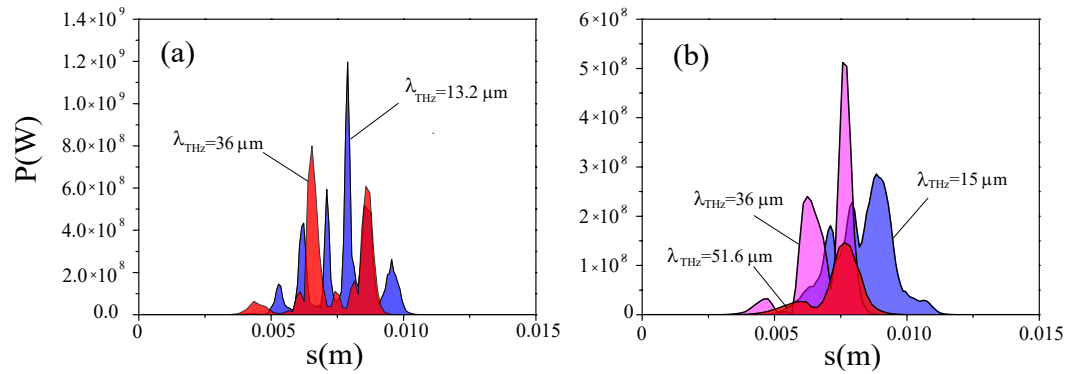


Figure 8. Intra-cavity radiation power profile $P(W)$ vs. coordinate $s(m) = t(s)c$. Window (a): undulator period $\lambda_w = 3.5$ cm; red curve: $\gamma = 55.5$, $\lambda = 36$ μm ; blue curve: $\gamma = 81.5$, $\lambda = 13.2$ μm . Window (b): undulator period $\lambda_w = 4.5$ cm; red curve: $\gamma = 65$, $\lambda = 51.6$ μm ; magenta curve: $\gamma = 55.5$, $\lambda = 36$ μm ; blue curve: $\gamma = 86$, $\lambda = 15$ μm .

Table 3. Intra-cavity radiation energy E_{IC} for the different normalised emittance of the electron beam ϵ_n and losses $L_c = L_{ext} + L_{mirr} + L_{lens}$.

ϵ_n (mm mrad)	1	1.4	1	1.4	1	1.4
L_c (%)	2	2	4	4	6	6
E_{IC} (mJ)	4.2	2.8	2.6	2	1.7	1.1

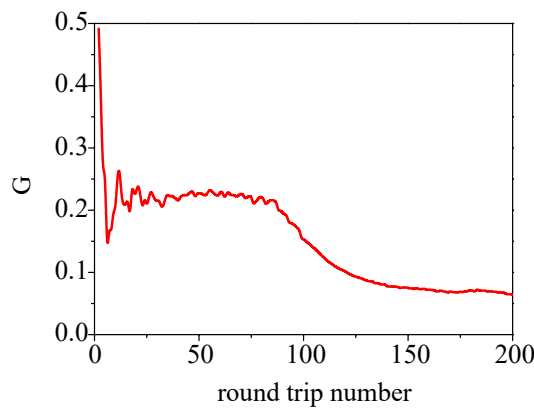


Figure 9. Radiation gain vs. number of round trip for the case with $\lambda = 15$ μm , losses at 6% and emittance of 1.4 mm mrad.

4. The TeraHertz Optical Cavity

The TeraHertz optical cavities of FEL oscillators in operation are usually stable cavities constituted by a front and a rear mirror, with the undulator in between. The example described here, instead, is a four-mirror unstable cavity in a bow-tie configuration sketched in Figure 10. The mirrors are spherical and constitute a telescopic system, surrounding the Compton IP, which provides the focusing needed for increasing the luminosity of the system. This cavity has been inspired by those currently used in Thomson scattering sources, for instance in BriXSiO [23] or ThomX [24]. Other solutions could, however, be exploited. The radiation exits the undulator (point 1) with an assigned waist size w_1 and curvature radius R_1 provided by the GENESIS 1.3 calculations.

The THz radiation must hit the holed front mirror with a size $w_2 (>> w_1)$ large enough to guarantee a fraction of a few percent of extra-cavity radiation with a hole with a radius of a few mm, namely $w_2 \simeq 10$ cm. For the THz pulse propagation, we follow the ABCD

model of the Gaussian beams. The length between the end of the undulator and the mirror (point 2) is then chosen in such a way that

$$w_2 = \sqrt{\left(1 + \frac{l_1 + l_2}{R_1}\right)^2 w_1^2 + \left(\frac{\lambda(l_1 + l_2)}{\pi w_1}\right)^2} \simeq 0.1 \text{ m}$$

Considering, for instance, the case with $\lambda = 15 \mu\text{m}$ and using the values of Table 2 for w_1 and R_1 ($w = 2\sigma$ and $R = \sigma/\theta_{div}$), the second term $\propto \lambda$ is negligible with respect to the first one, giving $(l_1 + l_2) \simeq (w_2/w_1 - 1)R_1 \simeq 13 \text{ m}$. A waist at the IP (point 6) of the order of $1.5 \times 10^{-4} \text{ m}$ entails a focusing distance $l_4 \simeq 3.14 \text{ m}$. The radiation reflected on mirror 1 should encounter a successive electron bunch in the IP, leading to $l_2 + l_3 + l_4 = m\Delta l$, where m is an integer number and Δl the bunch-to-bunch separation. With an angle of collision of 2° , $l_2 \simeq 2.6 \text{ m}$ and $l_3 \simeq 0.24 \text{ m}$. On the other hand, the total round trip length should also be an integer multiple n of Δl , namely $l_5 + l_6 + l_7 + l_u + l_1 \simeq n\Delta l$. The radiation should arrive consistently matched with the undulator (point 11). This condition is guaranteed by values of $w_{11} \simeq 7.510^{-3} \text{ m}$ and $R_{11} = -1 \text{ m}$, leading to $l_5 = 0.27 \text{ m}$, $l_6 = 14.72 \text{ m}$ and $l_7 = 0.24 \text{ m}$. The resulting round trip length is 36 m and the linear dimension of the cavity is approximately 18 m . The mirrors turn out to have the following curvature radii: $r_1 \simeq 27.3 \text{ m}$, $r_2 \simeq 3.14 \text{ m}$, $r_3 \simeq 0.27 \text{ m}$ and $r_4 = 0.39 \text{ m}$. Radiation with wavelengths up to $50 \mu\text{m}$ can be transported and focused with these same curvature lengths, by operating slight adjustments of the position of the mirrors. The considerable value of the power stored inside the Fabry–Pérot cavity could produce relevant thermal effects on the mirrors, inducing the deformation of their surfaces with an insurgence of transverse mode degeneracy. Methods for overcoming this issue are based on inducing losses to higher-order modes and have been studied in [24,42].

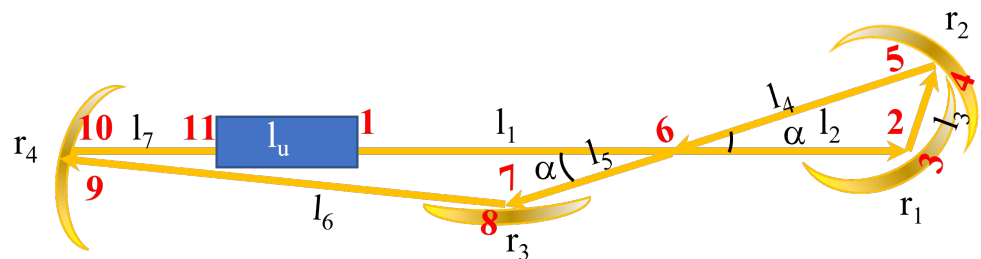


Figure 10. Dual source of THz and X-ray radiation. The cavity is constituted by four mirrors, one of them (r_1) holed for THz and X-ray extraction. Point 1: undulator exit. Point 2: arrival on mirror 1. Point 3: departure from mirror 1. Point 4: arrival on mirror 2. Point 5: departure from mirror 2. Point 6: interaction point. Point 7: arrival on mirror 3. Point 8: departure from mirror 3. Point 9: arrival on mirror 4. Point 10: departure from mirror 4. Point 11: undulator entrance. Electron beam and THz radiation interact at an angle α of few degrees.

5. The Inverse Compton Scattering Process: Numerical Results

The interaction between the electron beam and the THz radiation propagating backward was investigated with the classical model based on the Liénard–Wiechert potentials [43]. The double differential energy spectrum with respect to frequency ω and solid angle Ω is given by:

$$\frac{d^2W}{d\omega d\Omega} = \frac{e^2}{4\pi^2c} \left| \int_{-\infty}^{\infty} dt e^{i(\omega t - \underline{n} \cdot \frac{\underline{r}(t)}{c})} \left(\underline{n} \times \frac{(\underline{n} - \underline{\beta}) \times \dot{\underline{\beta}}}{(1 - \underline{n} \cdot \underline{\beta})^3} \right)_{ret} \right|^2 \quad (2)$$

where $\underline{r}(t)$ is the position of the electron, \underline{n} is the direction of the observer position, the index ret indicates that all the factors are evaluated at the retarded time, $\underline{\beta}$ and $\underline{\dot{\beta}}$ are the electron velocity and acceleration normalised to the speed of light, with

$$\underline{\dot{\beta}} = \frac{-e}{m_e c \gamma} \left[\underline{E}_L (1 - \underline{\beta} \cdot \underline{e}_k) + \underline{\beta} \cdot \underline{E}_L (\underline{e}_k - \underline{\beta}) \right]. \tag{3}$$

$E_L(x, y, z, t)$ is the electric field obtained by propagating the THz pulse generated by the FEL calculation shown in Figure 8 and \underline{e}_k is the direction of the interacting radiation.

The crucial need for focusing the THz radiation on the Compton IP derives from the dependence of the final X-ray yield on the rms pump transverse size σ_{THz} exhibited in Formula (1) and can be solved by the installation of the telescopic system based on mirrors in the scattering region.

As shown in the previous paragraph, the radiation in the IP can be focused down to $\sigma_{THz} \simeq 65 - 75 \mu\text{m}$ in the case of $\lambda_{THz} \simeq 13 - 15 \mu\text{m}$ and to about $150 - 250 \mu\text{m}$ for $\lambda = 36 - 51 \mu\text{m}$. Figure 11 presents the dependence of the total X-ray flux on the THz radiation size σ_{THz} for 3 nm of X-ray wavelength (window(a)) and 0.5 nm (window (b)). As can be seen, a suitable focus allows us to exceed 10^5 X-ray photon per shot. Figure 12 shows the number of photons N_X (solid lines, left axis) and the bandwidth b_w (dotted lines, right axis) obtained with different collimation angles θ_{coll} for the five cases analysed and for a THz focusing reference value $\sigma_{THz} \simeq 5 \lambda_{THz}$. The X-ray radiation bandwidths of the case analysed are all very similar except for a slight difference in the initial value, due to the different bandwidths of the THz pulses. The number of photons, instead, strongly depends on the THz intensities. The cases obtained with the shorter undulator period generate more intense X-rays.

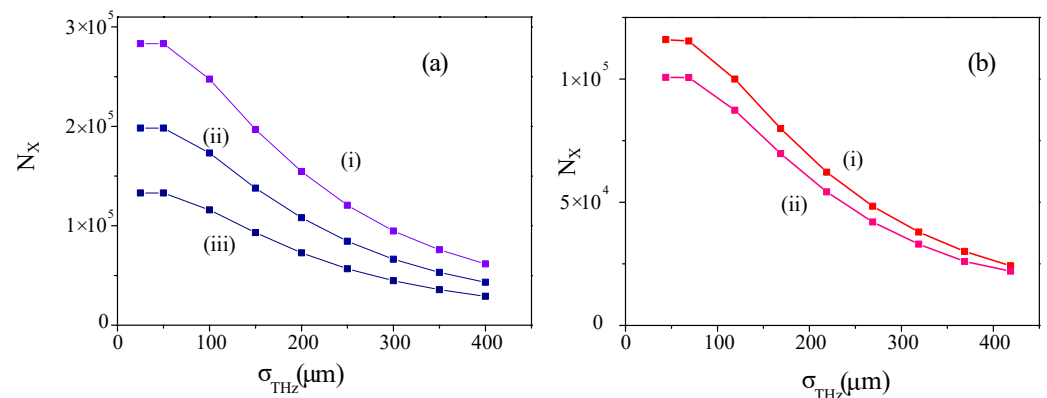


Figure 11. Total number of X-ray photons N_X as a function of rms dimension of the THz pulse in the IP, $\sigma_{THz}(\mu\text{m})$. Window (a): $\lambda_X = 3 \text{ nm}$, (i) $\lambda_w = 3.5 \text{ cm}$, $\lambda_{THz} = 36 \mu\text{m}$; (ii) $\lambda_w = 4.5 \text{ cm}$, $\lambda_{THz} = 36 \mu\text{m}$; (iii) $\lambda_w = 4.5 \text{ cm}$, $\lambda_{THz} = 51.6 \mu\text{m}$. Window (b): $\lambda_X = 0.5 \text{ nm}$, (i) $\lambda_w = 3.5 \text{ cm}$, $\lambda_{THz} = 13.2 \mu\text{m}$; (ii) $\lambda_w = 4.5 \text{ cm}$, $\lambda_{THz} = 15 \mu\text{m}$.

Table 4 collects information about the X-rays. The results were obtained by collimating the output yield in a proper angle $\theta_{coll} \simeq 10 \text{ mrad}$ for a bandwidth of approximately 10%. If broader or narrower spectra are required or tolerated, they can be achieved by varying the collimation angle, as presented in Figure 12. Usually, it is not possible to operate in the Fourier transform limit with Compton sources. The spectrum is indeed fixed at the zero order by the collimation system and could depend in a finer way on the emittance and energy spread of the electrons, while the length of the pulse is determined by the length of the electron beam. Jitters of the radiation follow those of the electron beam. Figure 13 shows the spectra of the X-ray radiation at 3 nm (window (a)) and 0.5 nm (window (b)) collimated at a bandwidth of 10% for the five reference cases. Figure 14 presents the effect of the presence of a collision angle. The case with $\lambda_{THz} = 15 \mu\text{m}$ and cavity losses $L_c = L_{ext} + L_{mirr} + L_{lens} = 2\%$, 4% and 6% was analysed as a function of the interaction

angle α ($\alpha = 0$ for head-to-head collisions). The data show a contained decrease in the photon number that remains quite negligible for angles below 5° . The Rayleigh length of the X radiation is of the order of tens of meters and its size on the front mirror much smaller than the dimension of the hole, allowing the extraction of the X-rays from the cavity without problems.

Table 4. X-ray radiation: electron energy, pump characteristics, results. Repetition rate of the source 5×10^7 Hz. IC: intra-cavity, EC: extra-cavity.

γ	e-Beam		55.5	81.5	65	55.5	86
λ_{THz}	THz	μm	36	13.2	51.6	36	15
E_{IC}	THz	mJ	3	3.38	1	2.1	2.8
N/shot	IC THz	$\times 10^{17}$	5.5	2.6	2.5	3.8	2.1
N/s	IC THz	$\times 10^{25}$	2.75	1.3	1.25	1.9	1.05
N/shot	EC THz	$\times 10^{15}$	11	5.2	5	7.6	4.2
N/s	EC THz	$\times 10^{23}$	5.5	2.6	2.5	3.8	2.1
size in IP	THz	μm	180	65	250	180	75
λ_X	X-ray	nm	3	0.5	3	3	0.5
N_X /shot	X-ray	$\times 10^5$	1.7	1.05	1.27	1.19	0.96
N_X /s	X-ray	$\times 10^{12}$	8.5	5.3	6.3	6	4.8
$N_{X, coll}$ /shot	X-ray	$\times 10^5$	0.41	0.42	0.23	0.29	0.37
$N_{X, coll}$ /s	X-ray	$\times 10^{12}$	2.2	2.25	1.15	1.45	1.85

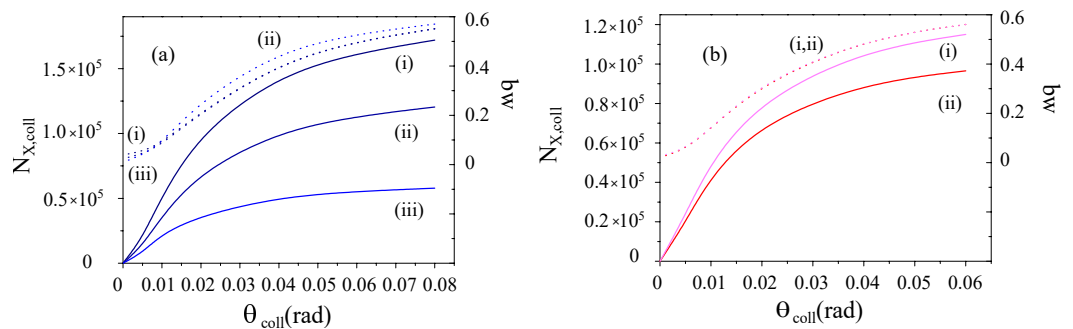


Figure 12. Number of photons $N_{X, coll}$ (solid lines) and bandwidth (dotted lines) as a function of collimation angle θ_{coll} (rad). Window (a): $\lambda_X = 3$ nm, (i) $\lambda_w = 3.5$ cm, $\lambda_{THz} = 36$ μm ; (ii) $\lambda_w = 4.5$ cm, $\lambda_{THz} = 36$ μm ; (iii) $\lambda_w = 4.5$ cm, $\lambda_{THz} = 51.6$ μm . Window (b): $\lambda_X = 0.5$ nm, (i) $\lambda_w = 3.5$ cm, $\lambda_{THz} = 13.2$ μm ; (ii) $\lambda_w = 4.5$ cm, $\lambda_{THz} = 15$ μm . In window (b), the bandwidths relevant to cases (i) and (ii) are not distinguishable.

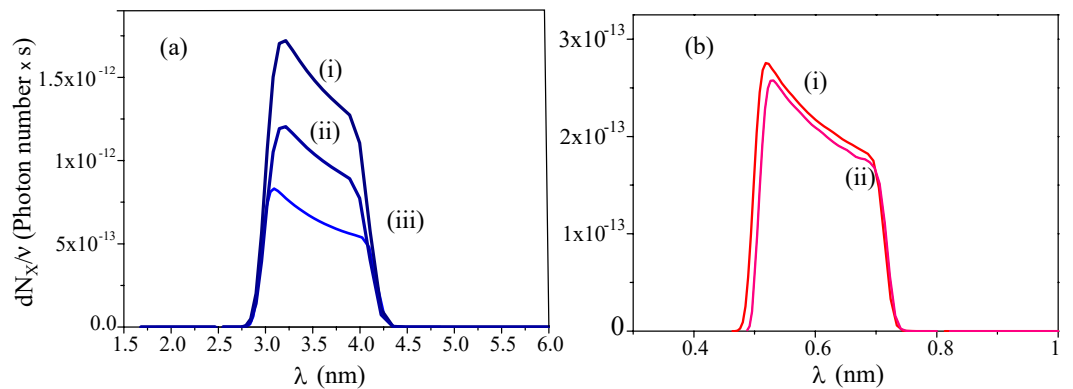


Figure 13. Spectrum of the collimated X-ray radiation for a bandwidth of 10%. Window (a): $\lambda_X = 3$ nm, (i) $\lambda_w = 3.5$ cm, $\lambda_{THz} = 36$ μm ; (ii) $\lambda_w = 4.5$ cm, $\lambda_{THz} = 36$ μm ; (iii) $\lambda_w = 4.5$ cm, $\lambda_{THz} = 51.6$ μm . Window (b): $\lambda_X = 0.5$ nm, (i) $\lambda_w = 3.5$ cm, $\lambda_{THz} = 13.2$ μm ; (ii) $\lambda_w = 4.5$ cm, $\lambda_{THz} = 15$ μm .

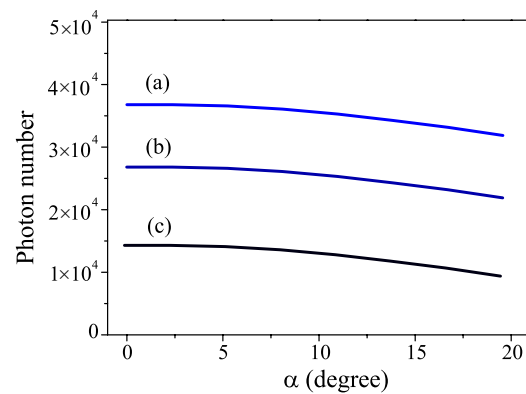


Figure 14. Number of photons of the collimated X-ray radiation for bandwidth at 10% as a function of the complementary angle α between the electron beam and THz radiation (head-to-head interaction $\alpha = 0$). $\lambda_w = 4.5$ cm, $\lambda_{THz} = 15$ μ m. $\lambda_X = 0.5$ nm, (a): $L_c = 2\%$, (b): $L_c = 4\%$, (c): $L_c = 6\%$.

6. Conclusions

The dual source we presented here, simultaneously delivering THz and X-ray radiation, has a compact footprint and can therefore be installed in medium-size laboratories, hospitals or university campuses. It is based on a relatively simple upgrade of a THz FEL oscillator, consisting in the addition of a telescopic system surrounding the Compton interaction point, placed in the centre of the cavity. A possible geometry of the cavity, a bow-tie configuration with four mirrors, was discussed. The undulator should occupy part of the region between the telescopic system and the front mirror. The dimension and cost of the device are almost the same as those of a THz oscillator. The THz radiation generated in an FEL oscillator propagating backward in the cavity hits a successive electron bunch producing soft X-rays via Thomson/Compton back-scattering. In this condition, THz FEL intracavity pulses with mJ-class energy at 15–50 microns of wavelength, driven by 20–100 MeV energy electron bunches, can deliver up to few 10^5 soft X-ray photons per shot by Compton back-scattering at a rate of 10–100 MHz, synchronised with the THz radiation. Two possible undulator choices at $\lambda_w = 3.5$ and 4.5 cm were described. The first one produces higher levels of THz radiation energy, with larger bandwidths and less regular power distributions. The second one, conversely, has smoother power density and narrower spectra, but the radiation yield features lower energy values. More than 10^{17} THz photons per shot are emitted intra-cavity by the FEL oscillator, meaning more than 10^{15} per shot to the extra-cavity users, and more than 10^5 X-ray photons being driven per shot. These numbers, multiplied by the repetition rate of the source, namely 10–100 $\times 10^6$ Hz, give 10^{22} – 10^{23} THz photons/s, coupled with more than 10^{12} X-ray photons/s. Open technological challenges are the implementation and the optimisation of the cavity elements, such as mirrors, lenses and windows, issues which should be studied within a work of conceptual and technical design. Lenses could also be made by artificial dielectric material [44]. For windows, instead, materials with maximum transparency in both THz and soft X-rays domains should be used. The problems of the transport and focusing of radiation pulses are, however, common to THz sources of all kinds and currently under study with increasing interest in the whole THz radiation community.

Author Contributions: Conceptualisation, V.P.; methodology, all authors; formal analysis, all authors; investigation, all authors; resources, all authors; data curation, all authors; writing—original draft preparation, all authors; writing—review and editing, all authors. All authors have read and agreed to the published version of the manuscript.

Funding: This research received no external funding.

Institutional Review Board Statement: Not applicable.

Informed Consent Statement: Not applicable.

Data Availability Statement: All data are available and could be asked to the Authors.

Conflicts of Interest: The authors declare no conflict of interest.

References

1. Turner, J.J.; Dakovski, G.L.; Hoffmann, M.C.; Hwang, H.Y.; Zarem, A.; Schlotter, W.F.; Moeller, S.; Minitti, M.P.; Staub, U.; Johnson, S.; et al. Combining THz laser excitation with resonant soft X-ray scattering at the Linac Coherent Light Source. *J. Synchrotron Radiat.* **2015**, *22*, 621–625. [CrossRef] [PubMed]
2. Hoffmann, M.C.; Turner, J.J. Ultrafast X-ray Experiments Using Terahertz Excitation. *Synchrotron Radiat. News* **2012**, *25*, 17–24. [CrossRef]
3. Zhang, Z.; Fisher, A.S.; Hoffmann, M.C.; Jacobson, B.; Kirchmann, P.S.; Lee, W.-S.; Lindenberg, A.; Marinelli, A.; Nanni, E.; Schoenlein, R.; et al. A high-power, high-repetition-rate THz source for pump–probe experiments at Linac Coherent Light Source II. *J. Synchrotron Radiat.* **2020**, *27*, 890–901. [CrossRef] [PubMed]
4. Zapolnova, E.; Golz, T.; Pan, R.; Klose, K.; Schreiber, S.; Stojanovic, N. THz pulse doubler at FLASH: Double pulses for pump–probe experiments at X-ray FELs. *J. Synchrotron Radiat.* **2018**, *25*, 39–43. [CrossRef]
5. Free-Electron Laser at Jefferson Laboratory, from ‘Jefferson Lab’. Available online: <https://www.jlab.org/FEL/> (accessed on 1 April 2021).
6. Ortega, J.M.; Glotin, F.; Prazeres, R. Extension in far-infrared of the CLIO free-electron laser. *Infrared Phys. Technol.* **2006**, *49*, 133–138. [CrossRef]
7. Oepets, D.; van der Meer, A.F.G.; van Amersfoort, P.W. The free-electron-laser user facility FELIX. *Infrared Phys. Technol.* **1995**, *36*, 293–308. [CrossRef]
8. Winnerl, S.; Stehr, D.; Drachenko, O.; Schneider, H.; Helm, M.; Seidel, W.; Michel, P.; Schneider, S.; Seidel, J.; Grafström, S.; et al. FELBE Free-Electron Laser: Status and Application for Time Resolved Spectroscopy Experiments. In Proceedings of the Joint 31st International Conference on Infrared and Millimeter Waves and 14th International Conference on Terahertz Electronics, Shanghai, China, 8–22 September 2006.
9. Bolotin, V.P.; Vinokurov, N.A.; Kayran, D.A.; Knyazev, A.; Kolobanov, E.I.; Kotenkov, V.V.; Kubarev, V.V.; Kulipanov, G.N.; Matveenko, A.N.; Medvedev, L.E.; et al. Status of the Novosibirsk Terahertz FEL. In Proceedings of the FEL Conference, Trieste, Italy, 29 August–3 September 2004; pp. 226–228.
10. Jeong, Y.U.; Lee, B.C.; Kim, S.K.; Cho, S.O.; Cha, B.H.; Lee, J.; Kazakevitch, G.M.; Vobly, P.D.; Gavrilov, N.G.; Kubarev, V.V.; et al. First lasing of the KAERI compact far-infrared free-electron laser driven by a magnetron-based microtron. *Nucl. Instrum. Methods Phys. Res. A* **2001**, *475*, 47–50. [CrossRef]
11. Isoyama, G.; Kato, R.; Kashiwagi, S.; Igo, T.; Morio, Y. Development of FEL and SASE in the far-infrared region at ISIR, Osaka University. *Infrared Phys. Technol.* **2008**, *81*, 371–374. [CrossRef]
12. Dou, Y.; Shu, X.; Yang, X.; Li, M.; Deng, D.; Wang, H.; Lu, X.; Xu, Z. Present status of CAEP THz FEL facility. In Proceedings of the 40th International Conference on Infrared, Millimeter, and Terahertz Waves (IRMMW-THz), Hong Kong, China, 23–28 August 2015.
13. Serafini, L. BriXSino Conceptual Design Report. 2021. Available online: <https://marix.mi.infn.it/brixsino-docs/> (accessed on 10 May 2022).
14. Petrillo, V.; Andreone, A.; Bacci, A.; Bosotti, A.; Broggi, F.; Drebot, I.; Galzerano, G.; Giannotti, D.; Giove, D.; Koral, C.; et al. High brilliance Free-Electron Laser Oscillator operating at multi-MegaHertz repetition rate in the short-TeraHertz emission range. *Nucl. Instrum. Methods A* **2022**, *1040*, 167289. [CrossRef]
15. Gadjev, I.; Sudar, N.; Babzien, M.; Duris, J.; Hoang, P.; Fedurin, M.; Kusche, K.; Malone, R.; Musumeci, P.; Palmer, M.; et al. Inverse free electron laser acceleration-driven Compton scattering X-ray source. *Sci. Rep.* **2019**, *9*, 532. [CrossRef]
16. Honda, Y.; Shimada, M.; Aryshev, A.; Kato, R.; Miyajima, T.; Obina, T.; Takai, R.; Uchiyama, T.; Yamamoto, N. Stimulated Excitation of an Optical Cavity by a Multibunch Electron Beam via Coherent-Diffraction-Radiation Process. *Phys. Rev. Lett.* **2018**, *121*, 184801. [CrossRef]
17. Koral, C.; Mazaheri, Z.; Papari, G.P.; Andreone, A.; Drebot, I.; Giove, D.; Masullo, M.R.; Mettievier, G.; Opromolla, M.; Paparo, D.; et al. Multi-Pass Free Electron Laser Assisted Spectral and Imaging Applications in the Terahertz/Far-IR Range Using the Future Superconducting Electron Source BriXSino. *Front. Phys.* **2022**, *10*, 725901. [CrossRef]
18. Gruner, S.M.; Bilderback, D.; Bazarov, I.; Finkelstein, K.; Krafft, G.; Merminga, L.; Padamsee, H.; Shen, Q.; Sinclair, C.; Tigner, M. Energy recovery linacs as synchrotron radiation sources (invited). *Rev. Sci. Instrum.* **2002**, *73*, 1402. [CrossRef]
19. Tigner, M. A Possible Apparatus for Electron Clashing-Beam Experiments. *Il Nuovo Cimento (1955-1965)* **1965**, *37*, 1228–1231. [CrossRef]
20. Cardarelli, P.; Bacci, A.; Calandrino, R.; Canella, F.; Castriconi, R.; Cialdi, S.; del Vecchio, A.; di Franco, F.; Drebot, I.; Gambaccini, M.; et al. BriXS, a new X-ray inverse Compton source for medical applications. *Phys. Med.* **2020**, *77*, 127–137. [CrossRef]
21. Drebot, I.; Bacci, A.; Bertucci, M.; Bosotti, A.; Broggi, F.; Canella, F.; Cialdi, S.; Citterio, M.; Ferragut, R.; Galzerano, G.; et al. BriXSino High-Flux Dual X-Ray and THz Radiation Source Based on Energy Recovery Linacs. In Proceedings of the IPAC 2022 13th International Particle Accelerator Conference, Bangkok, Thailand, 12–17 June 2022. [CrossRef]

22. Samsam, S.; Conti, M.R.; Rossi, A.R.; Bacci, A.; Petrillo, V.; Opromolla, M.; Ruijter, M.; Sertore, D.; Bosotti, A.; Paparella, R.; et al. The HOMEN model: An estimator of high order modes evolution in an energy recovery linac. In Proceedings of the Conference IPAC 2022 13th International Particle Accelerator Conference, Bangkok, Thailand, 12–17 June 2022. [CrossRef]
23. Suerra, E.; Giannotti, D.; Canella, F.; Drebot, I.; Capra, S.; Cipriani, D.; Mettevier, G.; Galzerano, G.; Cardarelli, P.; Cialdi, S.; et al. A new method for spatial mode shifting of stabilized optical cavities for the generation of dual-color X-rays. *Nucl. Instrum. Methods Phys. Res. Sect. A Accel. Spectrom. Detect. Assoc. Equip.* **2021**, *1019*, 165852. [CrossRef]
24. Dupraz, K.; Alkadi, M.; Alves, M.; Auguste, L.A.D.; Babigeon, J.-L.; Baltazar, M.; Benoit, A.; Bonis, J.; Bonenfant, J.; Bruni, C.; et al. The ThomX ICS source. *Phys. Open* **2020**, *5*, 100051. [CrossRef]
25. Weikum, M.; Akhter, T.; Alesini, D.; Alexandrova, A.; Anania, M.P.; Andreev, N.; Andriyash, I.; Aschikhin, A.; Aßmann, R.; Audet, T.; et al. Status of the Horizon 2020 EuPRAXIA conceptual design study. *J. Phys. Conf. Ser.* **2019**, *1350*, 012059. [CrossRef]
26. Serafini, L.; Bacci, A.; Bellandi, A.; Bertucci, M.; Bolognesi, M.; Bosotti, A.; Broggi, F.; Calandrino, R.; Camera, F.; Canella, F.; et al. MariX, an advanced MHz-class repetition rate X-ray source for linear regime time-resolved spectroscopy and photon scattering. *Nucl. Instrum. Methods Phys. Res. Sect. A Accel. Spectrom. Detect. Assoc. Equip.* **2019**, *930*, 167–172. [CrossRef]
27. Piovela, N.; Chaix, P.; Shvets, G.; Jaroszynski, D.A. Analytical theory of short-pulse free-electron laser oscillators. *Phys. Rev. E* **1995**, *52*, 5470–5486. [CrossRef]
28. Hajima, R.; Nagai, R. Generation of a Self-Chirped Few-Cycle Optical Pulse in a FEL Oscillator. *Phys. Rev. Lett.* **2003**, *91*, 024801. [CrossRef] [PubMed]
29. Curcio, A.; Dattoli, G.; Di Palma, E.; Petralia, A. Free electron laser oscillator efficiency. *Opt. Commun.* **2018**, *425*, 29. [CrossRef]
30. Bonifacio, R.; Pellegrini, C.; Narducci, L. Collective instabilities and high-gain regime in a free-electron Laser. *Opt. Commun.* **1984**, *50*, 373. [CrossRef]
31. Dattoli, G.; Ottaviani, P.L.; Pagnutti, S. Booklet for FEL Design: A Collection of Practical Formulae, ENEA RT/2007/40/FIM. Available online: www.fel.enea.it/booklet/pdf/Booklet_for_FEL_design.pdf (accessed on 1 March 2020).
32. Xie, M. Design Optimization for an X-ray Free Electron Laser Driven by SLAC Linac. 1996. Available online: <https://accelconf.web.cern.ch/p95/ARTICLES/TPG/TPG10.PDF> (accessed on 10 May 2022).
33. Ranjan, N.; Terzić, B.; Krafft, G.A.; Petrillo, V.; Drebot, I.; Serafini, L. Simulation of inverse Compton scattering and its implications on the scattered linewidth. *Phys. Rev. Accel. Beams* **2018**, *21*, 030701. [CrossRef]
34. Curatolo, C.; Drebot, I.; Petrillo, V.; Serafini, L. Analytical description of photon beam phase spaces in inverse Compton scattering sources. *Phys. Rev. Accel. Beams* **2017**, *20*, 080701. [CrossRef]
35. Reiche, S. GENESIS 1.3: A fully 3D time-dependent FEL simulation code. *Nucl. Instrum. Methods Phys. Res. Sect. A* **1999**, *429*, 243–248. [CrossRef]
36. Petrillo, V.; Opromolla, M.; Bacci, A.; Broggi, F.; Drebot, I.; Ghiringhelli, G.; Puppini, E.; Rossetti Conti, M.; Rossi, A.R.; Ruijter, M. et al. Coherent, high repetition rate tender X-ray Free-Electron Laser seeded by an Extreme Ultra-Violet Free-Electron Laser Oscillator. *New J. Phys.* **2020**, *22*, 073058. [CrossRef]
37. Opromolla, M.; Bacci, A.; Rossetti Conti, M.; Rossi, A.R.; Rossi, G.; Serafini, L.; Tagliaferri, A.; Petrillo, V. High Repetition Rate and Coherent Free-Electron Laser Oscillator in the Tender X-ray Range Tailored for Linear Spectroscopy. *Appl. Sci.* **2021**, *11*, 5892. [CrossRef]
38. Opromolla, M.; Petrillo, V. Two Color TeraHertz Radiation by a Multi-Pass FEL Oscillator. *Appl. Sci.* **2021**, *11*, 6495. [CrossRef]
39. Hajima, R.; Nishimori, N.; Nagai, R.; Minehara, E.J. Analyses of superradiance and spiking-mode lasing observed at JAERI-FEL. *Nucl. Instrum. Methods Phys. Res. A* **2021**, *475*, 270–275. [CrossRef]
40. Dattoli, G.; Torre, A.; Mezi, L.; Gallardo, J.C.; Caloi, R. Spectral structures of supermodes in free-electron lasers. *Phys. Rev. A* **1989**, *39*, 4281. [CrossRef]
41. Ottaviani, P.L.; Pagnutti, S.; Dattoli, G.; Sabia, E.; Petrillo, V.; van der Slot, P.J.M.; Biedron, S.; Milton, S. Deep saturated Free Electron Laser oscillators and frozen spikes. *Nucl. Instrum. Methods Phys. Res. Sect. A* **2016**, *834*, 108–117. [CrossRef]
42. Klaassen, T.; de Jong, J.M.; van Exter, J.P. Woerdman Transverse mode coupling in an optical resonator. *Opt. Lett.* **2005**, *30*, 1959–1961. [CrossRef]
43. Jackson, J.D. *Classical Electrodynamics*, 3rd ed.; John Wiley & Sons: New York, NY, USA, 1998; ISBN 978-0-471-30932-1.
44. Mendis, R.; Nagai, M.; Wang, Y.; Karl, N.; Mittleman, D.M. Terahertz Artificial Dielectric Lens. *Sci. Rep.* **2016**, *6*, 23023. [CrossRef]